Journal of Materials Chemistry A

ROYAL SOCIETY OF CHEMISTRY

PAPER

View Article Online
View Journal | View Issue

Cite this: J. Mater. Chem. A, 2022, 10, 16602

Pressure dependence on the three-dimensional structure of a composite electrode in an all-solid-state battery†

Yuya Sakka,[a] Hisao Yamashige,[b] Ayaka Watanabe,[a] Akihisa Takeuchi,[c] Masayuki Uesugi,[c] Kentaro Uesugi[c] and Yuki Orikasa *[a]

Received 24th March 2022
Accepted 8th July 2022

DOI: 10.1039/d2ta02378d

rsc.li/materials-a

An all-solid-state battery in which the organic liquid electrolyte of a lithium-ion battery (LIB) is replaced with an inorganic solid electrolyte is a candidate for next-generation rechargeable batteries. Although the solid electrolyte has high conductivity, its charge and discharge characteristics are inferior to those of conventional LIBs. To achieve the high performance of all-solid-state batteries, it is necessary to grasp the phenomena unique to the composite electrode that uses the solid electrolyte. This study analyses the three-dimensional structure of the composite electrode in an all-solid-state battery using a laboratory-built cell capable of performing electrochemical and X-ray computed tomography (CT) measurements while monitoring applied pressures. The dependencies of pressure on the porosity, contact area, and tortuosity of the composite electrodes are quantitatively analysed to evaluate their effects on the electrochemical properties. The CT observation reveals that there is insufficient contact between the active material and the solid electrolyte in a plane perpendicular to the pressure direction. The contact interface is found to be a key parameter for the charge/discharge characteristics.

Introduction

An all-solid-state battery (ASSB) using an inorganic solid electrolyte (SE) is expected to be safer than a conventional lithium-ion battery (LIB) equipped with an organic liquid electrolyte.[1] Furthermore, when a SE with a transport number of one is used, it is hardly affected by variation in the electrolyte salt concentration, which is a problem for liquid electrolytes,[2–5] and this improves the rate capability.[6] In addition, mechanically suppressing the dendrite formation that occurs in lithium metal anodes potentially improves its capacity retention and safety.[7,8] However, despite the discovery of SEs with high ionic conductivity,[9] in general the charge/discharge performance of all-solid-state batteries is lower than that observed in liquid electrolytes. In order to make the most of the advantages of an ASSB, it is necessary to understand the reaction mechanism within the electrode.

Since the electrochemical reaction of batteries proceeds at the two-dimensional electrode–electrolyte interface,[10] a composite electrode, which is a mixture of an active material (AM), an electrolyte, and a conductive additive, is used as the electrode of an ASSB to increase the effective reaction area. The available supply of ions and electrons in the composite electrode greatly affects the energy density, rate capability, and cycling performance of an ASSB. The ion and electron conduction pathways are related to the microstructure of the composite electrode,[11] and they depend on the engineering fabrication conditions, such as composition,[12–14] external press pressure,[15] binder,[16] coating,[17] *etc.* In LIBs using liquid electrolytes, the AM and electrolyte form an essentially sufficient interfacial connection. In contrast, in an ASSB, when the contacts between the AM and SE happen to be poor, the transportation of ions is restricted.[17–21] In other words, for an ASSB, along with the challenge of maximising the ion-transport pathways in composite electrodes, which it shares with LIBs, there is the added challenge of ensuring solid-to-solid contact, and both of these challenges need to be overcome.

Not only is high pressure applied during the preparation of ASSB electrodes, but pressure must be maintained during the charge/discharge reactions. The former is the fabrication pressure and the latter is the stack pressure. During electrode fabrication, high pressure is applied to improve solid-to-solid contact between powders, which involves plastic deformation within composite electrodes. Charge/discharge reaction causes a volume change in the AM, resulting in poor contact between AM and SE. On the other hand, stack pressure is necessary to maintain proper contact between the electrode and the SE. Based on the literature, the upper limit of the stack pressure is

[a]Department of Applied Chemistry, Ritsumeikan University, 1-1-1 Nojihigashi, Kusatsu, Shiga 525-8577, Japan. E-mail: orikasa@fc.ritsumei.ac.jp
[b]Toyota Motor Corporation, Toyota-cho, Toyota, Aichi 471-8571, Japan
[c]Japan Synchrotron Radiation Research Institute, 1-1-1 Kouto, Sayo, Hyogo 679-5198, Japan

† Electronic supplementary information (ESI) available. See https://doi.org/10.1039/d2ta02378d

suggested to be 1 MPa practically,[22] compared with the commonly used high fabrication pressure of approximately hundreds of MPa. The parameters of the pressure have a direct effect on the void fraction in the composite electrode and change the apparent ionic conductivity.[23–25] To optimise the performance of an ASSB, it is necessary to understand the effect of pressure on it. Previous studies on the correlation between stack pressure and the three-dimensional structure at the lithium anode and SE interface have shown that dendrite formation occurs at higher stack pressures.[26,27] On the cathode side, it has been shown that strain caused by the pressure reduces the contact between the AM and SE and determines the performance.[18,24]

Analysis of the three-dimensional structure has been carried out using focused-ion-beam scanning electron microscopy (FIB-SEM)[15,28] and X-ray computed tomography (CT).[25,29–33] In particular, in X-ray CT, there is the advantage that *operando* measurement can be performed while changing the pressure or allowing electrochemical measurement to proceed. This has already been shown to be useful for dendrite observation in SE[29–33] and electrode structure analysis of AM/SE.[18] The three-dimensional structure from X-ray CT data can be combined with the simulation to discuss the inhomogeneous charge/discharge mechanism.[34] Although it has become widely known that the pressure of an ASSB affects the three-dimensional structure, quantitative analysis of the cathode three-dimensional structure controlled by applied pressure, and direct observation of the anisotropy of the contact interface do not yet appear to have been fully explored. In this study, a cell capable of electrochemical and X-ray CT measurements is developed while controlling the applied pressure of an ASSB, and the dependency of the stack pressure on the three-dimensional structure of a cathode is quantified. It is directly observed that the contact between AM and SE is anisotropic with respect to the pressure, which is a phenomenon unique to an ASSB.

Experimental terms

The cathode AM, SE, and conductive agent were $LiNbO_3$-coated $LiNi_{0.33}Co_{0.33}Mn_{0.33}O_2$ (NCM), $Li_{10}GeP_2S_{12}$ (LGPS), and acetylene black (DENKA BKACK, Denka Co., Ltd) (AB), respectively. The coating was applied using a rolling fluidised coating machine (MP-01, Powrex) based on a procedure previously described in the literature.[35] LGPS was prepared *via* a solid-state reaction at 550 °C under an Ar flow. The scanning electron micrographs of NCM and LGPS are provided in Fig. S1 and S2 in the ESI.† These were mixed in a mortar in a glove box in an Ar atmosphere with a weight ratio of 1 : 1 : 0.1. For the anode, an In–Li alloy was formed by crimping a piece of In foil (Nilaco) with a piece of Li foil (Honjo Metal Co., Ltd). 1.0 mg of cathode composite, 1.0 mg of electrolyte, and In–Li foil were placed in a cylinder with a diameter of 1 mm. The inside of the cylinder was sealed with an O-ring during the measurements. The stack pressure was controlled using screws at the top of the cell. The In–Li|LGPS|NCM all-solid-state cells were placed under different pressures and were charged and discharged. The charge/discharge measurements of the prepared In–Li|LGPS|NCM were carried out at 298 K with different stack pressures using a battery test system (HJ1001SDE, Hokuto Denko Co., Ltd).

The X-ray CT measurements using a monochromatic X-ray beam were performed using beamline BL20XU of SPring-8, Japan with a beam energy of 20 keV. The undulator radiation X-ray beam was diffracted by using a Si (111) double-crystal monochromator. The detector was a visible-light conversion type X-ray detector using a CMOS camera (C13440-20CU, Hamamatsu Photonics K. K.) with a pixel size of *ca.* 0.5 μm and a field of view of *ca.* 1.0 × 1.0 mm. For each CT measurement, 1800 projections were collected with a 180° angular range for an exposure time of 0.05 s per frame. Segmentation and analysis of the 3D data were conducted using the Dragonfly 4.1 software (Object Research Systems, Montreal, Canada).

Results and discussion

An *operando* X-ray CT measurement cell with monitored applied pressure is illustrated in Fig. 1. The diameter of the electrode and electrolyte is 1 mm so that the X-ray at 20 keV can penetrate the electrode and electrolyte. These electrodes and electrolyte layers are pushed into the cylinder and pressed using an upper stainless-steel rod. The rod is also placed on the bottom side, which is in contact with the load-sensing transducer. The upper and bottom rods operate as the current collector. The charge/discharge measurement and X-ray CT measurement can be performed in the same cell while changing the pressure.

To investigate the relationship between applied pressure and charge/discharge characteristics, two sets of charge/discharge measurements are conducted. The first set is the cycles of charge/discharge measurements with a constant pressure of 6 MPa, with the results shown in Fig. 2a. Because a pressure of 6 MPa is very small, both the capacity and cycling performance are low. At low pressure, the contact between NCM and LGPS is insufficient. Then, the charge/discharge reaction of NCM proceeds only at specific spots where ionic current is supplied. Even if the stack pressure is maintained, the volume change of NCM results in a significant decrease in contact with LGPS at specific spots, which causes capacity fading. In this study, the loading of NCM is 60 mg cm^{-2}, which is much higher than the reported condition. This is due to the electrode diameter of 1 mm and the readability of the precision electronic balance. The thick

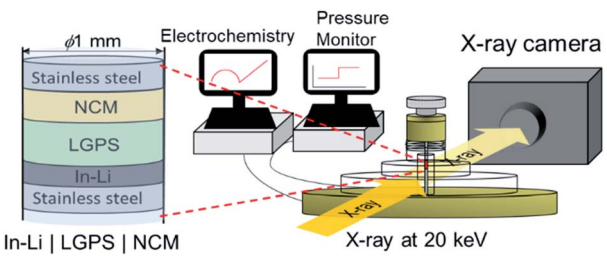

Fig. 1 Illustration of the X-ray CT measurement and an all-solid-state battery cell.

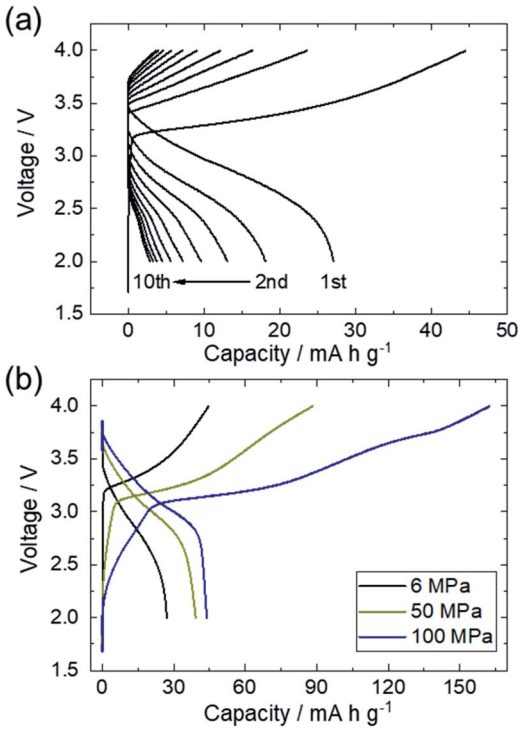

Fig. 2 (a) Charge/discharge cycle curves of an In–Li|LGPS|NCM all-solid-state battery using a laboratory-built measurement cell at a rate of 0.01C and stack pressure of 6 MPa. (b) Initial charge/discharge curves at a rate of 0.01C under various pressures.

composite electrode causes inhomogeneous charge/discharge reaction due to the high ionic resistance in through-plain direction. Fig. 2b shows the initial charge/discharge cycles of the different cells held under various pressures. For charge/discharge using LGPS electrolyte, irreversible capacity due to oxidative decomposition of the electrolyte is observed in the initial charge reaction,[36] which is also seen in the results of this experiment. Comparing the initial discharge reaction, which does not include the decomposed effect, the effect of pressure on discharge capacity can be seen in the range from 6 MPa to 100 MPa, indicating an increase in discharge capacity by applying pressure. We examined the pressure dependency using one cell, where the pressure is increased every two cycles for a total of 10 cycles (Fig. S3†). Two cycles of charge/discharge measurements at 6 MPa are first performed, and then two cycles are performed at a pressure of 12 MPa. The observed capacity also increases with respect to the applied pressure.

The previous study has reported that the specific capacity of all-solid-state batteries depends on the fabrication pressure, with the capacity decreasing at 50 MPa rather than 150 MPa.[15] Since no pressure was added during fabrication in our experiments, the pressure shown in this study corresponds to the previously reported fabrication pressure. In other words, the dependence of charge/discharge capacity on the pressure in a range below 100 MPa in this study is consistent with the results of the previous report.

Next, morphological changes in the composite electrode and the electrolyte under various pressures were analysed using X-ray CT. The reconstructed images of X-ray CT are provided in Fig. S4–S6.† The analysed area was 512 × 512 × 50 μm^3, which was cropped from the obtained three-dimensional images. The proportions of NCM, LGPS, and voids were identified based on the transmission intensity (Fig. S7–S11†). Their volume ratios, NCM/LGPS contact area, and the tortuosity of the LGPS connection pathway into the composite electrode were calculated.

The porosity and contact area fraction are important parameters involved in Li ion transport in the composite electrode and the effective area of the interfacial reaction between NCM and LGPS. Fig. 3a shows the pressure dependence on the porosity of the composite electrode and the SE layer. As the

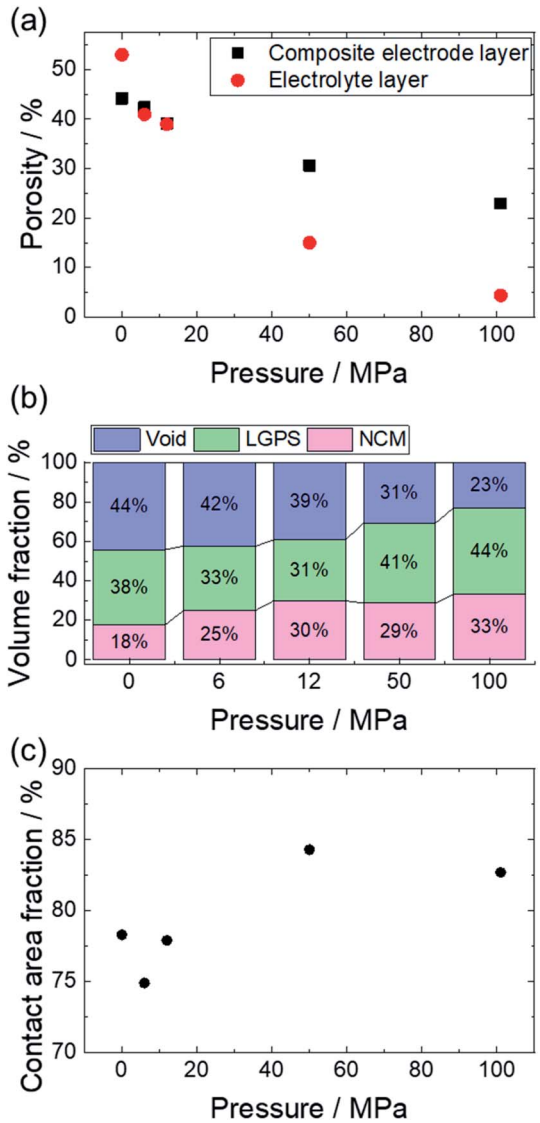

Fig. 3 (a) Pressure dependence on the porosity of the composite electrode and SE layer. (b) Volume fraction of NCM, LGPS, and voids in the composite electrode layer for various pressures. (c) Change in the NCM/LGPS contact area fraction as a function of pressure.

pressure increases, the porosity decreases in both, and there is no great difference between the composite electrode layer and the SE layer at pressures of less than 12 MPa. However, at high pressures, the pressure dependence of the porosity of the composite electrode is reduced. The porosities of the electrode and the electrolyte are 23% and 5% at a pressure of 100 MPa, respectively. There is a large difference between the composite electrode layer and the SE layer at a high pressure. This is caused by the presence of NCM particles, which exhibits a high Young's modulus[37] and large particle size (Fig. S1†). Hard NCM particles are slightly deformed by applied pressure and the NCM particle size is larger than that of LGPS, resulting in more voids around the NCM particles. Fig. 3b shows the volume change of NCM, LGPS, and voids in the composite electrode layer. The proportion of LGPS decreases while the proportion of NCMs increases up to a pressure of 12 MPa. In composites with different Young's moduli, large pressures can be applied to materials that have larger Young's moduli.[25] Hard NCM particles have small deformations in response to pressure, and, for uniaxial pressing, high pressure makes LGPS compress around the NCM particles in addition to reducing porosity. This also causes the soft LGPS to contract,[38] thus reducing the apparent volume fraction. When the pressure exceeds 12 MPa, the volume of NCM does not increase, and the porosity decreases due to the increasing LGPS. The particle size of the NCM particles is on the order of 10 μm, and any increase in the volume ratio levels off due to difficulties in deformation. LGPS with a smaller grain size and Young's modulus can fill the voids located around the NCMs. The volume ratio of NCM and LGPS does not follow the relative modulus because the direction of pressure is in one direction, and the particle size and shape are also different between NCM and LGPS. Thus, the process of densification in the composite electrode proceeds through two stages.

The void ratio on composite electrodes is changed by the particle size of AM. We examined X-ray CT analysis of the $LiFePO_4$ (LFP) electrode as the composite electrode with hundreds of nanometer-sized particles of AM (Fig. S12†). The void ratio is approximately 5% at 50 MPa, which is much lower than that of the micron-sized NCM electrode. This result implies that the small particles can fill the large void spaces. However, note that the small size of LFP particles tends to form nanoscale voids, which is challenging to quantify correctly due to the resolution of X-ray CT.

The contact area fraction represents the fraction of the area in contact between NCM and LGPS with respect to the surface area of the NCM particles (Fig. S13†). The contact area between NCM and LGPS serves as a reactive area for charge-transfer during charge/discharge. Fig. 3c shows the change in the NCM/LGPS contact area fraction as a function of pressure, along with the changes corresponding to the two-stage process described earlier. The fraction increases by approximately 10% when the pressure is greater than 50 MPa compared with the state under a pressure less than or equal to 12 MPa. At low pressures, the NCM particles are pressurised preferentially,[24] and so contact with the surrounding LGPS is not increased; however, at high pressures, LGPS fills the voids around the NCM particles, resulting in an increased contact area. On the other hand, the improvement in the contact area fraction stopped when the pressure reached 50 MPa. After 50 MPa, there is a small change in the volume of the voids, but no change in the contact area fraction. In addition, we compared X-ray CT images of the composite electrode under 50 MPa press and at 0 MPa after 50 MPa press (Fig. S14†). No clear changes were detected with respect to the void in the pressure-released condition.

During uniaxial pressing, the anisotropy phenomenon occurs within the contacted state between NCM and LGPS. Fig. 4a shows the XY, YZ, and XZ slices highlighting only the contact surface of the NCM particles. Green and blue lines indicate the NMC/LGPS contacted interface and the NCM/void interface, respectively. The relationship between the XZ plane and the pressure direction is shown in Fig. 4b. The contacted NCM/LGPS interface only serves as a pathway for Li-ion conduction to the AM. Detailed observations of these images reveal that the NCM particles have good contact with LGPS in the *Z*-axis direction, which is the pressure direction. On the other hand, preferential contact with the voids is observed in the horizontal direction, which is not the pressure direction. Such anisotropy of the contacted interface is predominantly

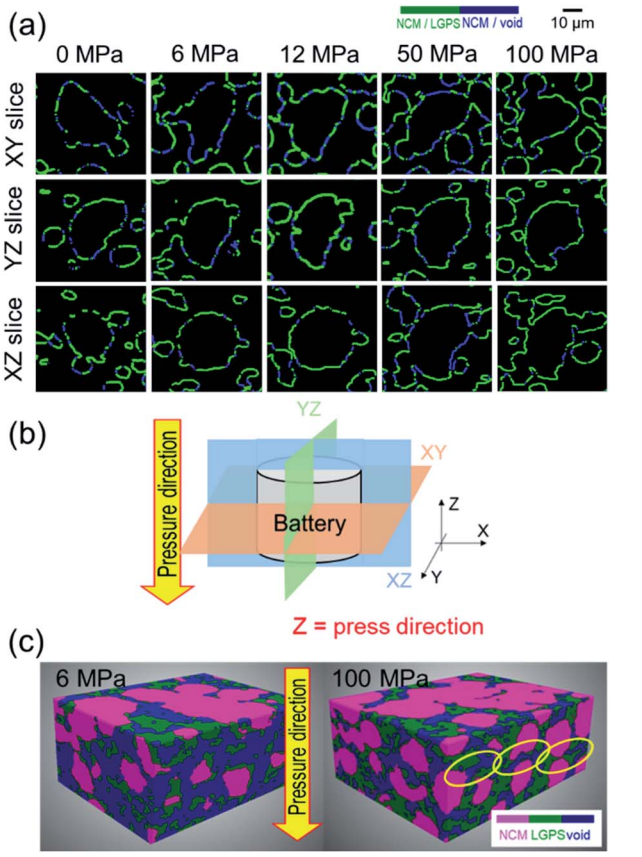

Fig. 4 (a) XY, YZ, and XZ slices highlighting only the contact surfaces of the NCM particles at various pressures. Green and blue lines indicate the NMC/LGPS contacted interface and the NCM/void interface, respectively. (b) XYZ axis and pressure direction. (c) Reconstructed three-dimensional image of the composite electrodes at stack pressures of 6 MPa and 100 MPa.

observed at low pressures, but also even at high pressures, though less frequently. Therefore, it can be concluded that NCM does not have good contact with LGPS horizontally, even at high pressures. In addition, as shown in Fig. 4c, many voids in the horizontal direction can be confirmed and the shape of the voids depends on the pressure direction. Therefore, void formation in the composite electrode and the contacted surface state of the NCM particles corresponds well to the pressure direction.

The tortuosity of the lithium-ion pathway in the composite electrode was subsequently calculated. Fig. 5a shows the analysed area, which was 36 × 36 × 50 μm^3, cropped from the obtained three-dimensional composite electrode images. In the calculation, a three-dimensional pathway connected by SE particles was extracted in the composite electrode (Fig. 5a), and this value was divided by the thickness of the observed region (Fig. 5b). Fig. 5c shows a histogram of the tortuosity for each pressure. Since the reported tortuosity of all-solid-state battery electrodes ranges from 1 to 10,[21,34,39–42] this study discusses a relative comparison with the pressure. The graph shows the flexural index on the horizontal axis and the frequency on the vertical axis. The mode value at each pressure value is highlighted with a red circle and the minimum value with a blue circle. Minimum and mode values decrease with increasing pressure. In contrast, when the pressure was 100 MPa, the tortuosity had increased and so had the variation. This mechanism will be discussed later.

The AC impedance measurement was simultaneously performed with the X-ray CT measurements. The pressure dependence on the apparent conductivity and the charge-transfer resistance estimated from the Nyquist plot (Fig. S15 and S16†) are provided in Fig. 6a and b, respectively. The apparent conductivity increases almost linearly with increasing pressure. This corresponds well to the behaviour of the porosity reduction as shown in Fig. 3a. The analysis of only the SEs has shown that the apparent conductivity increases due to a decrease in the porosity.[43] On the other hand, the charge transfer resistance is inversely proportional to the pressure. This corresponds to the increase of the contact area fraction of NCM/LGPS as shown in Fig. 3b. That is, under a high-pressure condition, a good NCM/LGPS interface is formed, which leads to a decrease in the charge-transfer resistance. The increase in the capacity of the charge/discharge reaction (Fig. 1) is mainly attributed to the improved interface between NCM and LGPS, resulting in a reduction of the charge-transfer resistance.

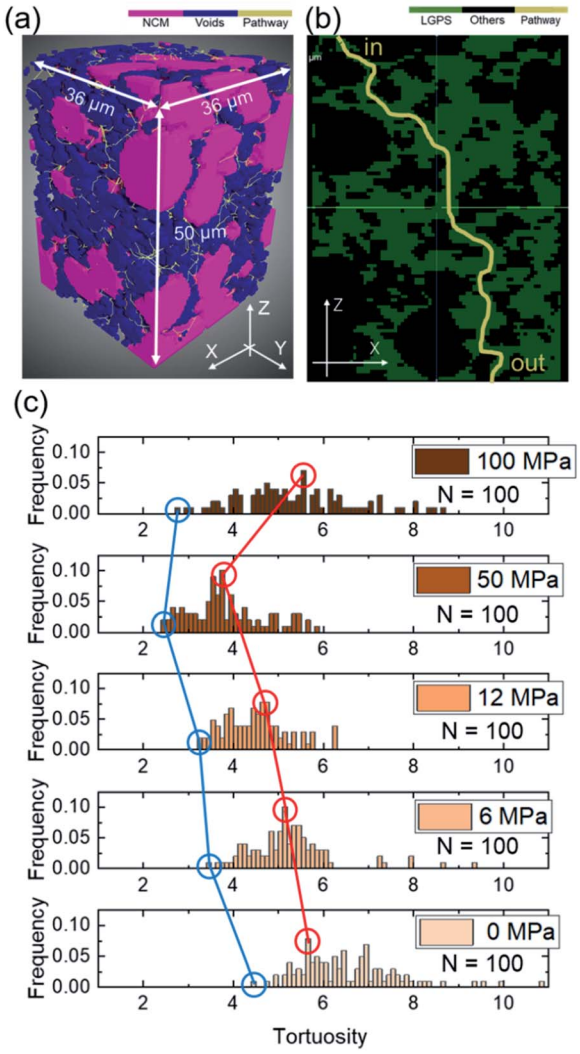

Fig. 5 (a) Cropped part of the obtained three-dimensional composite electrode images used to calculate the tortuosity. (b) Two-dimensional schematic view used to calculate the tortuosity. (c) Histogram of tortuosity for various pressures.

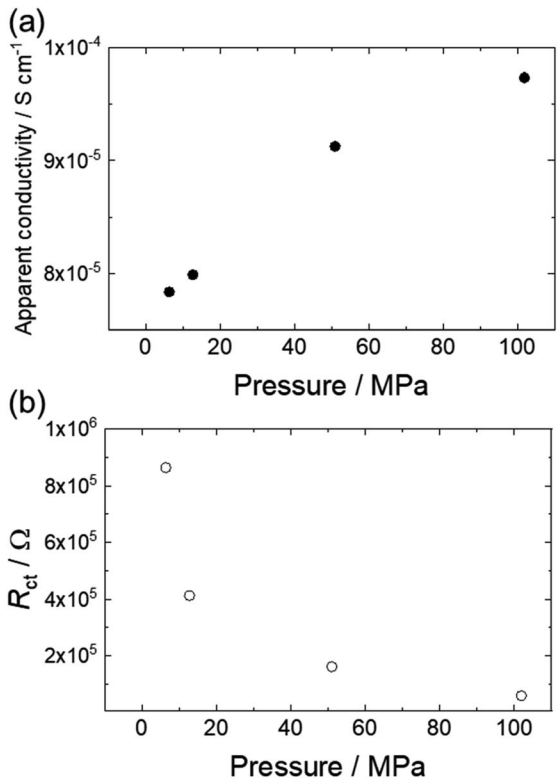

Fig. 6 (a) Apparent conductivity and (b) charge transfer resistance estimated by AC impedance as a function of pressure.

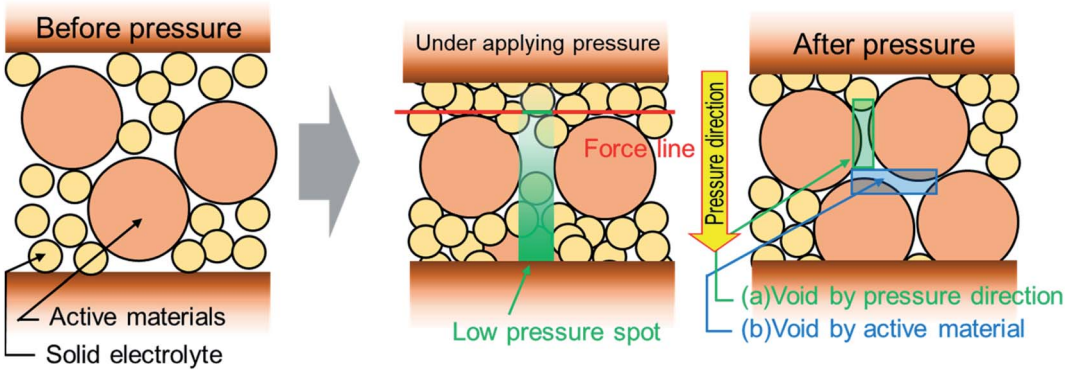

Fig. 7 Schematic illustration of morphological structural changes in a composite electrode by pressure application.

Based on these results, the effects of the AMs in the composite electrode will be discussed. The experimental findings outlined above lead to the morphological changes evident in the pressed composite electrode shown in Fig. 7. Although uniaxial pressing preferentially pushes the NCM particles, owing to their large Young's modulus,[37] the pressure of the flat current collector is not sufficiently applied to the space between the AM particles when the AMs are dense. Therefore, low-pressure spots are created in the gaps in the AM, and thus the SE does not fill these gaps, even after pressure is applied. The insufficient contact in the horizontal direction between the AMs and the electrolytes is caused by these low-pressure spots. Since no force is applied from the horizontal direction, the gap cannot be fully filled. In addition, even where the AMs overlap, the SEs cannot be filled and the voids remain. The unique hardness of the AM causes a difference in the porosity between the composite electrode layer and the SE layer, or else it prevents the composite electrode layers from being kept in contact with each other in the horizontal direction. Under uniaxial pressing, the voids in the composite electrodes that contain AMs have a large Young's modulus that is not sufficiently reduced.

The AMs affect the tortuosity of the composite electrodes. With regard to the pressure dependence of tortuosity, it has been confirmed that the tortuosity increases at 100 MPa. There are two factors that change the tortuosity in composite electrodes: it decreases with the increased volume of the void and increases with the increased volume of the AMs. Both of them exhibit a change in the opposite direction with respect to pressure, and therefore, at the same pressure, the behaviour of the tortuosity is reversed. For small-sized voids, large NCMs act as obstacles in the Li-ion pathway. Therefore, at 100 MPa when the AMs are well filled, the effect of increasing the AM is superior to the effect of decreasing the porosity, resulting in high tortuosity. The results indicate a reduced change in the minimum value of the tortuosity but do indicate an increase in the average tortuosity. It has been reported that the ionic conduction path provided by SE is the rate-limiting factor in high-rate charge/discharge.[44] Therefore, the increase of the tortuosity reduces the effective ionic conductivity, which directly leads to a decrease in rate capability. High-pressure fabrication of the composite electrodes causes such an increase in tortuosity, suggesting the trade-off between the connectivity of AM/SE and the tortuosity of SE. However, it is expected that the increase in tortuosity will have a minor impact on the electrochemical properties, since the pressure dependence of the charge/discharge measurement does not exhibit significant differences at pressures above 50 MPa.

Conclusions

This study used X-ray computed tomography to analyse the effects of pressure on the morphological structure of the composite electrode and electrochemical properties of an all-solid-state battery (ASSB) cell. It was found that increasing the pressure decreased the porosity and improved the contact area fraction between the active material (AM) and the solid electrolyte (SE), while the decrease in porosity impacted the apparent conductivity. The enhanced contact area fraction between the AM and SE led to an order of magnitude reduction in charge transfer resistance. The logarithmic increase of the charge/discharge capacity with the increase in pressure was attributed to both the improvement in apparent conductivity and the reduction in charge transfer resistance, but the effect of the charge transfer resistance reduction was particularly dominant. The contact interface between the AM and the SE was marginally perpendicular to the applied pressure. By improving the contact interface in the vertical direction, that is, by realising the contact between the AM and the SE in a three-dimensional manner, it is expected that the charge/discharge characteristics of ASSBs can be improved even at low pressures.

Author contributions

Y. S. and Y. O. conceived the study and conducted the *operando* X-ray CT experiments. H. Y. designed the *operando* measurement cell. Y. S. performed the charge/discharge test and analysed the X-ray CT data. A. W. examined the effect of the particle size on the void ratio. A. T., M. U. and K. U. assisted with the use of beamline BL20XU and reconstruction processing. Y. S. and Y. O. wrote the manuscript with input from all authors.

Conflicts of interest

The authors declare no conflicts of interest associated with this manuscript.

Acknowledgements

This work was partially supported by JSPS KAKENHI Grant Number 19H02694, and the New Energy and Industrial Technology Development Organization (NEDO), JPNP20004. The synchrotron radiation experiments were performed at the BL20XU of SPring-8 with the approval of the Japan Synchrotron Radiation Research Institute (JASRI) (Proposal No. 2019B1726, 2020A0502, 2021A1005, 2021A1539, and 2021B1724).

Notes and references

1 K. Takada, *Acta Mater.*, 2013, **61**, 759–770.
2 M. Klett, M. Giesecke, A. Nyman, F. Hallberg, R. W. Lindström, G. Lindbergh and I. Furó, *J. Am. Chem. Soc.*, 2012, **134**, 14654–14657.
3 S. A. Krachkovskiy, J. D. Bazak, P. Werhun, B. J. Balcom, I. C. Halalay and G. R. Goward, *J. Am. Chem. Soc.*, 2016, **138**, 7992–7999.
4 D. Takamatsu, A. Yoneyama, Y. Asari and T. Hirano, *J. Am. Chem. Soc.*, 2018, **140**, 1608–1611.
5 J. I. G. Dawkins, M. Z. Ghavidel, D. Chhin, I. Beaulieu, M. S. Hossain, R. Feng, J. Mauzeroll and S. B. Schougaard, *Anal. Chem.*, 2020, **92**, 10908–10912.
6 Y. Kato, S. Hori, T. Saito, K. Suzuki, M. Hirayama, A. Mitsui, M. Yonemura, H. Iba and R. Kanno, *Nat. Energy*, 2016, **1**, 7.
7 D. Cao, X. Sun, Q. Li, A. Natan, P. Xiang and H. Zhu, *Matter*, 2020, **3**, 57–94.
8 S. Yang, M. Takahashi, K. Yamamoto, K. Ohara, T. Watanabe, T. Uchiyama, T. Takami, A. Sakuda, A. Hayashi, M. Tatsumisago and Y. Uchimoto, *Solid State Ionics*, 2022, **377**, 115869.
9 N. Kamaya, K. Homma, Y. Yamakawa, M. Hirayama, R. Kanno, M. Yonemura, T. Kamiyama, Y. Kato, S. Hama, K. Kawamoto and A. Mitsui, *Nat. Mater.*, 2011, **10**, 682–686.
10 Y. Orikasa, K. Yamamoto, T. Shimizu and Y. Uchimoto, *Chem. Phys. Rev.*, 2022, **3**, 011305.
11 Y. Orikasa, Y. Gogyo, H. Yamashige, M. Katayama, K. Chen, T. Mori, K. Yamamoto, T. Masese, Y. Inada, T. Ohta, Z. Siroma, S. Kato, H. Kinoshita, H. Arai, Z. Ogumi and Y. Uchimoto, *Sci. Rep.*, 2016, **6**, 26382.
12 W. Zhang, D. A. Weber, H. Weigand, T. Arlt, I. Manke, D. Schröder, R. Koerver, T. Leichtweiss, P. Hartmann, W. G. Zeier and J. Janek, *ACS Appl. Mater. Interfaces*, 2017, **9**, 17835–17845.
13 Y. J. Nam, D. Y. Oh, S. H. Jung and Y. S. Jung, *J. Power Sources*, 2018, **375**, 93–101.
14 Y. Kimura, M. Fakkao, T. Nakamura, T. Okumura, N. Ishiguro, O. Sekizawa, K. Nitta, T. Uruga, M. Tada, Y. Uchimoto and K. Amezawa, *ACS Appl. Energy Mater.*, 2020, **3**, 7782–7793.
15 J. M. Doux, Y. Y. C. Yang, D. H. S. Tan, H. Nguyen, E. A. Wu, X. F. Wang, A. Banerjee and Y. S. Meng, *J. Mater. Chem. A*, 2020, **8**, 5049–5055.
16 K. Chen, S. Shinjo, A. Sakuda, K. Yamamoto, T. Uchiyama, K. Kuratani, T. Takeuchi, Y. Orikasa, A. Hayashi, M. Tatsumisago, Y. Kimura, T. Nakamura, K. Amezawa and Y. Uchimoto, *J. Phys. Chem. C*, 2019, **123**, 3292–3298.
17 J. Wu, S. Liu, F. Han, X. Yao and C. Wang, *Adv. Mater.*, 2021, **33**, 2000751.
18 H. Fathiannasab, L. K. Zhu and Z. W. Chen, *J. Power Sources*, 2021, **483**, 229028.
19 G. Bucci, B. Talamini, A. Renuka Balakrishna, Y.-M. Chiang and W. C. Carter, *Phys. Rev. Mater.*, 2018, **2**, 105407.
20 T. Li, H. Kang, X. Zhou, C. Lim, B. Yan, V. De Andrade, F. De Carlo and L. Zhu, *ACS Appl. Mater. Interfaces*, 2018, **10**, 16927–16931.
21 S. Choi, M. Jeon, J. Ahn, W. D. Jung, S. M. Choi, J.-S. Kim, J. Lim, Y.-J. Jang, H.-G. Jung, J.-H. Lee, B.-I. Sang and H. Kim, *ACS Appl. Mater. Interfaces*, 2018, **10**, 23740–23747.
22 M. J. Wang, E. Kazyak, N. P. Dasgupta and J. Sakamoto, *Joule*, 2021, **5**, 1371–1390.
23 H. Fathiannasab, A. G. Kashkooli, T. Y. Li, L. K. Zhu and Z. W. Chen, *J. Electrochem. Soc.*, 2020, **167**, 100558.
24 A. Ohashi, M. Kodama, X. Y. Sun, S. Hori, K. Suzuki, R. Kanno and S. Hirai, *J. Power Sources*, 2020, **470**, 228437.
25 A. Ohashi, M. Kodama, N. Horikawa and S. Hirai, *J. Power Sources*, 2021, **483**, 229212.
26 J. M. Doux, H. Nguyen, D. H. S. Tan, A. Banerjee, X. F. Wang, E. A. Wu, C. Jo, H. D. Yang and Y. S. Meng, *Adv. Energy Mater.*, 2020, **10**, 1903253.
27 C. Hansel and D. Kundu, *Adv. Mater. Interfaces*, 2021, **8**, 2100206.
28 T. Hamann, L. Zhang, Y. H. Gong, G. Godbey, J. Gritton, D. McOwen, G. Hitz and E. Wachsman, *Adv. Funct. Mater.*, 2020, **30**, 1910362.
29 J. Tippens, J. C. Miers, A. Afshar, J. A. Lewis, F. J. Q. Cortes, H. P. Qiao, T. S. Marchese, C. V. Di Leo, C. Saldana and M. T. McDowell, *ACS Energy Lett.*, 2019, **4**, 1475–1483.
30 S. Hao, J. J. Bailey, F. Iacoviello, J. F. Bu, P. S. Grant, D. J. L. Brett and P. R. Shearing, *Adv. Funct. Mater.*, 2021, **31**, 2007564.
31 J. A. Lewis, F. J. Q. Cortes, Y. Liu, J. C. Miers, A. Verma, B. S. Vishnugopi, J. Tippens, D. Prakash, T. S. Marchese, S. Y. Han, C. Lee, P. P. Shetty, H. W. Lee, P. Shevchenko, F. De Carlo, C. Saldana, P. P. Mukherjee and M. T. McDowell, *Nat. Mater.*, 2021, **20**, 503–510.
32 M. Otoyama, M. Suyama, C. Hotehama, H. Kowada, Y. Takeda, K. Ito, A. Sakuda, M. Tatsumisago and A. Hayashi, *ACS Appl. Mater. Interfaces*, 2021, **13**, 5000–5007.
33 N. Seitzman, O. F. Bird, R. Andrykowski, S. Robbins, M. M. Al-Jassim and S. Pylypenko, *ACS Appl. Energy Mater.*, 2021, **4**, 1346–1355.
34 A. Neumann, S. Randau, K. Becker-Steinberger, T. Danner, S. Hein, Z. Y. Ning, J. Marrow, F. H. Richter, J. Janek and A. Latz, *ACS Appl. Mater. Interfaces*, 2020, **12**, 9277–9291.

35 N. Ohta, K. Takada, I. Sakaguchi, L. Zhang, R. Ma, K. Fukuda, M. Osada and T. Sasaki, *Electrochem. Commun.*, 2007, **9**, 1486–1490.
36 T.-T. Zuo, R. Rueß, R. Pan, F. Walther, M. Rohnke, S. Hori, R. Kanno, D. Schröder and J. Janek, *Nat. Commun.*, 2021, **12**, 6669.
37 E. J. Cheng, K. Hong, N. J. Taylor, H. Choe, J. Wolfenstine and J. Sakamoto, *J. Eur. Ceram. Soc.*, 2017, **37**, 3213–3217.
38 D. A. Weber, A. Senyshyn, K. S. Weldert, S. Wenzel, W. Zhang, R. Kaiser, S. Berendts, J. Janek and W. G. Zeier, *Chem. Mater.*, 2016, **28**, 5905–5915.
39 L. Froboese, J. F. v. d. Sichel, T. Loellhoeffel, L. Helmers and A. Kwade, *J. Electrochem. Soc.*, 2019, **166**, A318–A328.
40 P. Minnmann, L. Quillman, S. Burkhardt, F. H. Richter and J. Janek, *J. Electrochem. Soc.*, 2021, **168**, 040537.
41 H. Fathiannasab, A. Ghorbani Kashkooli, T. Li, L. Zhu and Z. Chen, *J. Electrochem. Soc.*, 2020, **167**, 100558.
42 X. Lu, A. Bertei, D. P. Finegan, C. Tan, S. R. Daemi, J. S. Weaving, K. B. O'Regan, T. M. M. Heenan, G. Hinds, E. Kendrick, D. J. L. Brett and P. R. Shearing, *Nat. Commun.*, 2020, **11**, 2079.
43 A. Sakuda, A. Hayashi and M. Tatsumisago, *Sci. Rep.*, 2013, **3**, 2261.
44 A. L. Davis, V. Goel, D. W. Liao, M. N. Main, E. Kazyak, J. Lee, K. Thornton and N. P. Dasgupta, *ACS Energy Lett.*, 2021, **6**, 2993–3003.